Mesoporosity in doped silicon nanowires from metal assisted chemical etching monitored by phonon scattering

William McSweeney[1], Colm Glynn[1], Hugh Geaney[1], Gillian Collins[1,3], Justin D. Holmes[1,2,3], and Colm O'Dwyer[1,2]*

[1] *Department of Chemistry, University College Cork, Cork, T12 YN60, Ireland*

[2] *Micro-Nano Systems Centre, Tyndall National Institute, Lee Maltings, Cork, T12 R5CP, Ireland*

[3] *AMBER@CRANN, Trinity College Dublin, Dublin 2, D02 PN40, Ireland*

To whom correspondence should be addressed: E-mail: c.odwyer@ucc.ie; Tel: +353 (0)21 4902732; Fax: +353 (0)21 4274097

Abstract

Si NWs are shown to develop internal mesoporosity during metal assisted chemical etching from Si wafers. The onset of internal porosity in n^+-Si(100) compared to p-Si(100) is examined through a systematic investigation of etching parameters (etching time, $AgNO_3$ concentration, HF % and temperature). Electron microscopy and Raman scattering show that specific etching conditions reduce the size of the internal Si nanocrystallites in the internal mesoporous structure to 3-5 nm. Mesoporous NW are found to have diameters as large as 500 nm, compared to ~100 nm for p-NW that develop surface roughness. Etching of Si (111) wafers results in <100> oriented NWs forming a three-fold symmetrical surface texture, without internal NW mesoporosity. The vertical etching rate is shown to depend on carrier concentration and degree of internal mesoporosity formation. Raman scattering of the transverse optical phonon and photoluminescence measurements confirm quantum size effects, phonon scattering and visible intense red light emission between 685-720 nm in internally mesoporous NWs associated with the etching conditions. Laser power heating of NWs confirms phonon confinement and scattering, which is demonstrated to be a function of the internal mesoporosity development. We also demonstrate limitation of mesoporosity formation in n^+-Si NWs and development of

porosity within p-Si NW by controlling etching conditions. Lastly, the data confirm that phonon confinement and scattering often reported for Si NWs is due to surface-bound and internal nanostructure, rather than simply a NW diameter reduction in NW materials.

I. Introduction

Metal assisted chemical etching (MACE) allows for large-scale, and rapid fabrication of high-quality[1], well-aligned vertically oriented Si NWs with large areal homogeneity and tunable depths, which for a given etching bath can be affected by substrate doping type and doping concentration. The control of porosity in Si and controlled NW growth top-down has been beneficial for Li-ion batteries[2-10] thermoelectrics[11, 12], solar cells[13], and developments for artificial leaf and water oxidation[5] and electroluminescent devices.

Electrochemical etching can fine tune the direction and size of pore growth[14], which defines the remaining skeletal material of a range of semiconductors such as Si, but also III-Vs such as InP[15-23] and GaAs. MACE, however, can result in high sidewall roughness, and the control of this surface roughness and the development of internal mesporosity[24-26] are key challenges for reproducible large scale formation of functional nanoscale Si. The doping density of the Si plays a major role in defining the type of etching[27], and the resulting morphology for many of the parameters that affect the electrochemistry and etching of Si.[28, 29] The final Si nanostructure generated can be controlled by the substrate doping type level.[30-35]

Porous Si via MACE is conventionally made from highly doped Si ($>10^{17}$ cm^{-3}). It was found that with increasing doping level the Si NWs resulting from the MACE process become rougher and eventually porous.[31, 36-39] A key requirement for electroless etching methods is the need to control the degree of pore formation[40, 41].

During etching, Ag nanoparticles at the roots of the NWs (NW-substrate interface) can be converted into Ag^+ ions by H_2O_2.[37, 39] At a low H_2O_2 concentration, the generated Ag^+ ions can be again reduced to Ag during further Si oxidation and etching. Hole injection via an electroless process is thus continued as the Ag^+ is again reduced causing bond breaking of Si surface atoms through nucleophilic attack. Therefore porous Si NWs can be achieved for lightly doped wafers at a high H_2O_2 concentration.[42]

The direction of Si NWs relative to the surface is also important for Si NW based solar cells[43] and Si NW based field effect transistors[44, 45] and sensors. Initial reports showed that etching in (100) and (111) Si occurred in the vertical direction only.[46, 47] However more recently, contradicting reports stated that slanted NWs have been produced from these orientations.[43, 46-50] Recently, it was found that (100) wafers with resistivity of 6–8 Ω·cm relieve vertical <100> NWs at a relatively low volumetric ratio of HF/H_2O_2 of 3:1 while <111> NWs are generated when the HF concentration is increased.[38] Oxidation-rate-dependent etching can affect the resulting orientation of NWs, and changes in these parameters could likely modulate zig-zag growth directions top-down[51-53], akin to bottom-up VLS methods for kinked NWs.[54]

Raman scattering has been found to be an effective method for analyzing the optical and acoustic phonons in Si NWs[55] especially since phonon transport is fundamentally linked to crystal size, crystallinity, and scattering promoters such as defect, porosity or surface roughness.[12, 30, 35, 56] There are several causes of a redshift of a Raman peak, such as: a rise of temperature, high carrier densities, quantum confinement effects and stress in the Si NWs.[57-60]

High doping levels in n^+-NWs with sizes greater than their Bohr Radius may reduce the band gap, increasing the total power absorbed and therefore increasing the temperature of the NWs further[61]. Thermalized phonons that undergo confinement correspond to a reduced

thermal conductivity, inherently linked to the doping condition and the crystalline structure. Controlling the internal crystal structure through porosity or defect inclusion, and altering the surface roughness of Si NWs can allow quantum confinement tunability in thermal conductance and photoluminescence emission in nanoscale Si.

There are few formal investigations of the influence of doping concentration and doping type for both roughness and porosity formation[62] *within* NWs, in addition to the etching relief of the NWs themselves. Here, we report an investigation into the development of mesoporosity in Si NW layers using two markedly difference conductivity wafers: p-Si(100) with and n^+-Si(100) and n-Si(111) by varying the etching conditions used in a MACE process. An increase in the etching time produces longer Si NWs with low doped Si producing longer NWs than highly doped Si. The development of mesoporosity as a function of etching conditions are monitored by changes in phonon transport and scattering mechanisms by Raman scattering measurements and photoluminescence confirms the nanoscale nature of internal nanocrystallites within the mesoporous n^+-Si NWs. The data is correlated to detailed electron microscopy examination of the microstructure. We also show that a similar change in porosity is not attained for lower doped Si. Direct laser heating during Raman scattering measurements shows that the increasingly mesoporous Si NWs contribute to a greater shift in the transverse optical phonon and increased FWHM of this mode when compared to the less porous Si NWs.

II. Experimental

100 mm p-type B-doped Si(100) wafers (365 μm thickness) with a resistivity of 1 – 30 Ω·cm corresponding to a doping density of between 1.6 – 7.0 × 10^{14} cm^{-3}, n^+-Si(100) wafers, As-doped with resistivity in the range 0.001 – 0.005 Ω·cm corresponding to a doping density of between 1.2 – 7.4 × 10^{19} cm^{-3}, and n-Si (111) wafers, P(phosphorous)-doped with resistivity in the range 10.5 – 17.5 Ω·cm corresponding to a doping density of between 2.5 – 4.3 × 10^{14} cm^{-}

^{3} were used. The substrates were immersed for a variety of times (15 mins – 3 h) in a heated solutions with HF added (by volume) in the range 2.5 % – 20 % HF (denoted as %HF in the text), containing $AgNO_3$ (0.01 – 0.05 mol dm^{-3}) and maintained at varying temperatures between 25 °C and 75 °C using a thermostated water bath. The standard etching conditions were 1 h, 10 % HF, 0.02 mol dm^{-3} $AgNO_3$ at 50 °C. When one of the etching parameters was being varied, the other three etching parameters were kept at the standard etching condition. After removing the substrates from the etching bath they were washed copiously with deionized water and then with concentrated nitric acid to remove remnant Ag deposits.

Scanning electron microscopy (SEM) of cleaved (011) cross-sections and (001) plan view of the Si NWs were examined on a Hitachi S4800 FESEM operating at 5 kV. TEM was conducted at 200 kV using a JEOL TEM JEM-2100. The NWs were scraped into an IPA solution and dispersed onto holey carbon copper grids for analysis. Raman scattering spectroscopy was collected with a Renishaw InVia Raman spectrometer using a 514 nm 30 mW Argon ion laser with a nominal power of 30 mW, and spectra were collected using a RenCam CCD camera. The beam was focused onto the samples using either a 20× or 50× objective lens. The incident power of the laser was adjusted using calibrated filters. Photoluminescence (PL) were acquired using an excitation provided by a 325 nm emission from a cw He-Cd laser with power density of 2 W/cm^2. PL spectra were acquired using a Horiba iHR320 spectrometer equipped with a Synapse CCD matrix.

III. Results and discussion

Top-down Etching of Porous NW Layers

From SEM data, Fig. 1 shows that the length of the Si NWs formed from the highly doped n^+-Si(100) varies with etching time, but the etched morphology (porous surface topology) remains consistent. The NWs formed are perpendicular to the surface due to the preferred [100] etching

direction caused by HF dissolution of Si oxidized by the Ag nanoparticles (NPs) via an anionic SiF_6^{2-}. The NWs are observed to clump more as they increase with length as expected from capillary forces, but internal porosity weakens the structure of thicker n^+- mesoporous NWs. p-NWs also form similar arrays, as seen in Fig. 1(b) but without clumping. In Fig. 1(c), Si NWs are etched from Si(111) substrates. A detailed SEM study is provided in the Supporting Information, Section S1, Figs S1-S4.

Figure 1 (and Figs S1-S4) demonstrate the characteristic difference in array uniformity and morphology of NW layers from each different wafer type and orientation. As the fast etch direction in Si is the [100], Si NWs in Fig. 1 are perpendicular to the (100) surface. However MACE is maintained in the <100> direction(s) in Si(111), and NWs form a defined angle to the substrate. The plan-view images show the NWs facing three distinct directions in relation to each other, delineated by the relative reactivity of the Si in <111> versus <100> directions. While III-V semiconductors have different etch rates depending on whether the surface is III-atom or V-atom terminated[63] the anisotropy is Si etching is related to the effective H-passivation of {111}[5, 12] surfaces acting as stop planes, facilitating preferential etching along the three crystallographically equivalent [100], [010] and [001] directions. Unlike [100] oriented nominally parallel NWs etched from Si(100) substrates that are susceptible to clumping when either porous and/or of high aspect ratio, [100] NWs formed from Si(111) substrates do not clump, irrespective of their length.

Si NW layers etched from Si(111) substrates do not have uniform NW-substrate interfaces and due to the three relative orientations of NWs. Cross-sectional data in Fig. 1(c) and Fig. S4 shows that as the NWs increase in length (greater etch depth), the relief of the tri-directional morphology is such that any cross-section will have deeper regions where the angled NW orientation is parallel to the cleave plane. The magnified plan-view image of the Si NWs formed from the Si(111) wafer shows they form a three-fold symmetry. Considering the

(111) surface orientation and that the plan-view image comprises NWs that are oriented out of the plane of the image, all wires have a general [100] orientation. [31, 64] Lee et al. [64] reported that in Si(111), Au particles caused etching at approximately 55º to the surface in [100] direction. A p-Si (111) wafer also produced Si NWs at an angle of 40º to the substrate surface in the <100> direction.[65] It was also demonstrated that changes to the etching direction in n-Si(111) was possible by varying the HF:$AgNO_3$ ratio, temperature and etching time. The etching direction of the Ag particles was shown to be <111>, <110>, <211>, <311> and zigzag depending on the etching conditions.[66]

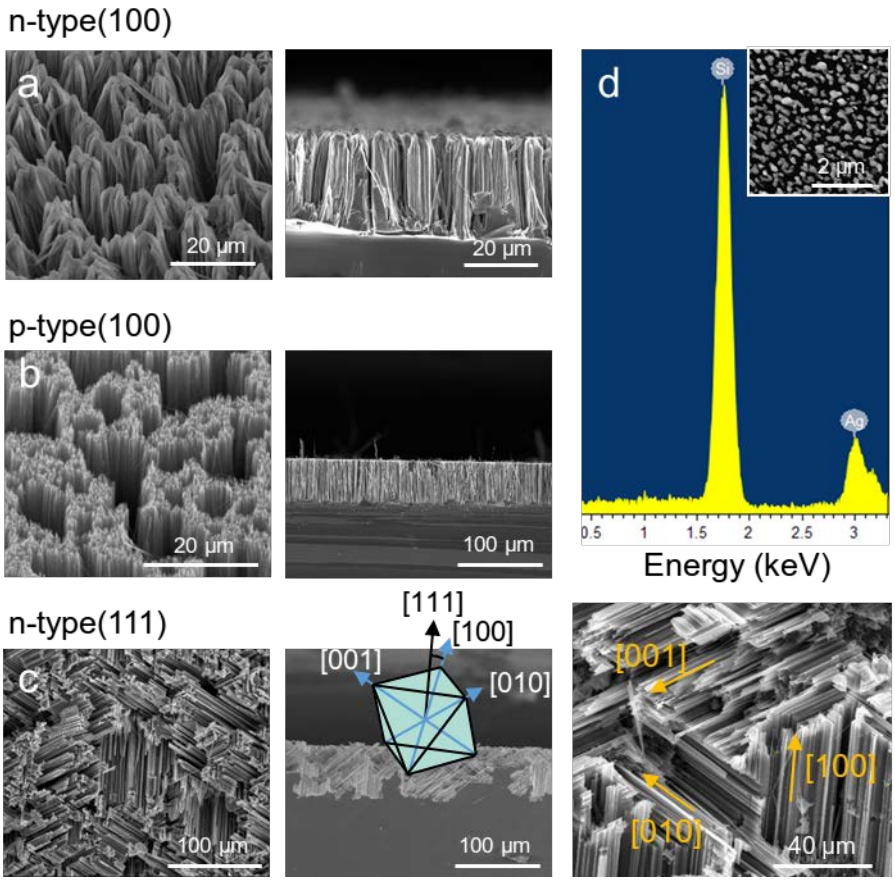

Figure 1. SEM images of MAC etched (a) n^+-Si(100) NWs (1.2 – 7.4 × 10^{19} cm^{-3}), (b) p-Si(100) (1.6 – 7.0 × 10^{14} cm^{-3}) and (c) n-Si(111) wafers (2.5 – 4.3 × 10^{14} cm^{-3}). A magnified image of the n-Si(111) NWs indicating the NW orientations post etching with respect to the (100) substrate. The schematic defines the orientations of Si NWs from Si(111) wafers as defined by the octahedral (111) diamond cubic cleavage plane. (d) EDX point mapping and associated SEM images of Ag nanoparticles by electroless deposition on the Si surface after 10s immersion.

Nanoparticle coarsening and agglomeration on the Si surface during the initial stages is believed to cause the non-uniformity in porosity, i.e. larger regions of efficient dissolution take place, whereas NW regions occur from more sparsely distributed, smaller Ag NP clusters. This distribution of etching also influences the degree of clumping. In the MAC approach reported here, Fig. 1(d) confirms that a random distribution of reduced Ag particles forms on the Si surface after 10 s immersion in the Ag^+-containing solution.

Since etching is preferential along the <100> directions, the relative length of low-doped p- and highly doped n^+-NWs from Si(100) and n-NWs from Si(111) were examined. Figure 2 is a plot of the measured NW length by SEM as a function of etching time for n^+- and p-(100) and n-(111) Si NWs.

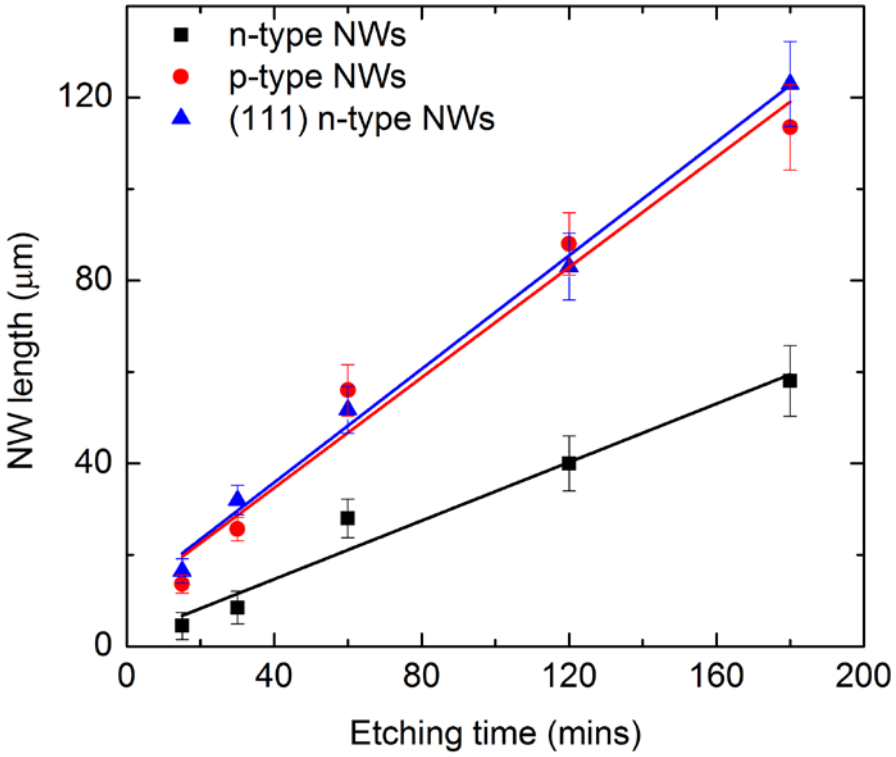

Figure 2. NW length vs etching time for highly doped n^+-Si(100), low doped p-Si(100) and low doped n-Si(111). Measurements for NW formed on Si(111) were taken along their entire length.

NWs etched from each type of substrate exhibit linear electroless etching rates. Both p-NWs from Si(100) surfaces and n-Si(111) NWs on exhibit near-identical lengths and etch rates

(0.87 and 0.81 μm/min, respectively). n^+-NWs on the other hand, etch more slowly at 0.33 μm/min. The faster etch rate for the p-Si NWs is a consequence of the higher majority carrier hole density. Thus, the etch rate of n-Si(111) is similar to p-Si(100). The similarity between n-Si(111) and p-Si(100) cannot be explained by relative hole concentrations alone. Whether SiH bonds passivate (111) faces until a hole is available for nucleophilic Si-Si bond attack during the electroless dissolution, or whether other proposed mechanism that consider H:Si(111) planes being etch-stop planes, the electroless process is still limited by hole concentration. For Si(111) wafers, the NWs are observed to be relieved at an angle equivalent to the separation between {111} and {100} planes. While the NW length is commensurate with etching time and rate, the depth of the entire layer is thus less (via Pythagorean geometry) than NWs formed perpendicularly to a Si(100) surface. Thus, the NW surface on Si(111) approximates a roughness planar surface rather than a high aspect ratio vertical NW surface. The NW layer on (111) surface is fully open to the electrolyte. Upon drying, the capillary forces found in parallel vertical dense NW arrays prevents clumping in n-Si(111) NW layers.

The etching rate is observed to be slower for the n^+-Si when compared to the p-Si, but NW length, as relieved during etching, increases linearly with time in all cases. As discussed earlier, some of MACE processes in the vertical direction (on (100) surface) cause Ag to diffuse out and re-deposit on the NW sidewalls. The n^+-NWs are internally mesoporous whereas the p-NWs are solid.[67] The etch rate is affected by several parameters. The anodic and cathodic bias of p- and n-type wafers respectively (versus Ag^+ reduction) defines the rate generation of holes and electrons that cause nucleophilic and electrophilic bond breaking. Unlike electrochemical etching, electroless etching requires the presence of the Ag^+ cathode in the reaction – complete dissolution is prevented by the 'dead' layer formed within the mesoporous nanocrystalline structure at sizes less than the depletion layer width. Figure 2 shows the etched depth (or NW length) as determined for each wafer type from SEM examination. Separately,

effects of minority carrier diffusion have been known to contribute to sidewall and further etching in some cases.[68, 69] Here, Ag-mediation MACE in a non-vertical direction in highly doped Si is possible compared to low doped Si due to the higher carrier concentration and narrower depletion region under opposite bias condition at the Si/electrolyte interface. However, for a finite and consistent density of Ag^+, less Ag contributes to the vertical etching, resulting in a slower vertical etch rate for n^+-Si as seen in Fig. 2.

Assuming a consistent surface porosity between p- and n^+-NWs from Si(100) surfaces (Figs 1 and 3), the relative difference in NW lengths can provide as estimate of differences in NW porosity, i.e. for an equally efficient electroless etching process, the NW length indicated the depth of etching

$$d_{NW,p/n} = QV_{M,Si}/nF \quad (1)$$

where Q is the total charge corresponding to the etching, $V_{m,Si}$ is the molar volume of Si, n is the number of electrons involved in the electroless process (n = 4) and F is Faradays constant. Without hole generation from peroxide reduction in this particular reaction, the mechanism is assumed to follow

$$Si + 6HF \rightarrow SiF_6^{2-} + 6H^+ + 4e^- \quad (2)$$

at the anode. Where the total etched volume of Si within the layer is similar, a % effective porosity increase in n^+-NWs is $d_{NW,n}/d_{NW,p} \sim 260\%$. While the n^+-NWs are likely more porous than this value (from TEM analysis), they are wider than p-NWs and consequently have a lower volumetric density within the etched region.

Phonon Scattering and Confinement in Mesoporous Si NWs

Examination of phonon scattering characteristics using Raman scattering measurements allows direct comparison between changes in internal and surface structure or morphology of NWs as a function of etching processes. Figure 3(a) shows a Raman scattering spectrum of the p- and the n^+-Si(100) NWs after 1 h of etching, and is consistent with the Raman spectra of crystalline

Si and porous Si.[70] The Raman shift relationship with crystallite size within the mesoporous nanowire structure is estimated by the following relation[71, 72]:

$$\Delta\omega(D) = -A(\frac{a}{D})^{\gamma} \quad (3)$$

where $\Delta\omega(D)$ is the Raman shift in a nanostructure of diameter D, a is the lattice constant of Si (a = 0.543 nm), and A = 47.41 cm^{-1} and γ = 1.44 are fit parameters that describe the phonon confinement in nanostructures of diameter D.

A clear peak shift and broadening of the TO phonon is found for n^{+}-NWs, indicative of phonon scattering mechanisms with contributions from confinement effects from nanoscale Si structure below the mean free path length of the TO phonon. The TO phonon observed (512 cm^{-1}) is red-shifted (from crystalline Si (520 cm^{-1}))[73, 74]. These phonon modes shift away from the Brillouin zone center ($q \neq q_0$) as crystal momentum is no longer conserved, causing the shift and asymmetric widening of the TO phonon to lower frequencies. Additionally, contributions to asymmetry and shifts in the TO phonon can also occur due to internal boundary scattering and surface scattering from rough NW edges. The shape of the phonon mode influence by quantum confinement effects is described by

$$I(\omega) = \int \frac{d^3 q C(0,q)^2}{[\omega - \omega(q)]^2 + \left(\frac{\Gamma_0}{2}\right)^2} \quad (4)$$

where ω(q) is the phonon dispersion curve (q, the phonon wave vector); Γ_0 is the natural linewidth = 4.6 cm^{-1} for Si at RT (inversely proportional to the intrinsic phonon lifetime); C(0,q) is the coefficient describing the phonon confinement at q_0 = 0, which is appropriate for first-order Raman scattering. The dispersion relation, $\omega(q) = \omega(TO)(1 - 0.25q^2)$ accounts for the size distribution of the nanocrystalline regions within the mesoporous NWs and the frequency of the roughness that contributes to phonon scattering. The integration is be performed over the entire Brillouin zone with the confinement function was chosen to be Gaussian as

$$|\mathrm{C}(0,q)|^2 = \exp\left(\frac{-q^2\mathrm{L}^2}{16\pi^2}\right) \quad (5)$$

where *L* is a parameter describing the grain size with a unit of *a*, where *a* is the lattice constant of crystalline silicon. The TO phonon for crystalline Si(100) is located at 520.2 cm^{-1} with a full-width at half-maximum (FWHM) of 4.6 cm^{-1}, and as shown in Fig. 3(a), the TO phonon of Si NWs is at 516.2 cm^{-1} with a FWHM of 14.2 cm^{-1}. Following Eqn (3), the reduction in crystalline grain size results from a larger frequency shift of the TO mode with associated broadening and asymmetric profile. The relation predicts a crystallite size of 2.9 – 3.1 nm, which is in good agreement with HRTEM data of the internal skeletal Si nanocrystal structure within mesoporous NWs. In Fig. 3(b), an increased redshift and broadening of the TO phonon mode is observed when the n^+-NWs etched for longer durations as more internal mesoporosity develops in time.

As the p-NWs are solid (i.e. non porous) with limited surface roughness (whose rms values that do not contribute significantly to surface phonon scattering[75]), there is no appreciable shift or asymmetric broadening of the TO mode observed (Fig. 3(c)) after extended etching periods [55, 58, 76]. In our case, internal mesoporosity in n^+-Si NWs from (100)-oriented substrates dominates scattering and phonon confinement, even in wires of larger diameter (n^+-NWs here can be ~5× wider than p-NWs, but internally mesoporous), and thus nanoscale features are a requirement for significant Raman mode shifts. Depending on the catalyst type and etching conditions, NWs formed exhibit either rough (high rms roughness >5 nm with a range of roughness frequencies) or smooth surfaces. One hypothesis states that Ag nanoparticles can disintegrate, detach or leach, diffuse outward, redeposit randomly and sink into the newly formed NWs surfaces continuously during the entire process of MACE process to induce a secondary etching step on the NW sidewalls to form pits.[31, 38, 42, 53] Chern et al.[38] stated that the holes generated in the MACE reaction can diffuse out before the primary reaction (vertical etching of the Si) and contribute to etching of the Si sidewalls resulting in the

porous Si NWs (Fig. 3(e)). This mechanism agrees with our previous work[67] wherein highly doped Si has facilitates a faster reaction rate than the p-Si because high carrier concentration favours charge transfer. In addition, as shown in [67] higher doped n^+-Si has a much narrower depletion region, allows tunneling of carriers and etching of the internal Si structure to much smaller dimensions, as evidenced by the Raman scattering characterization.

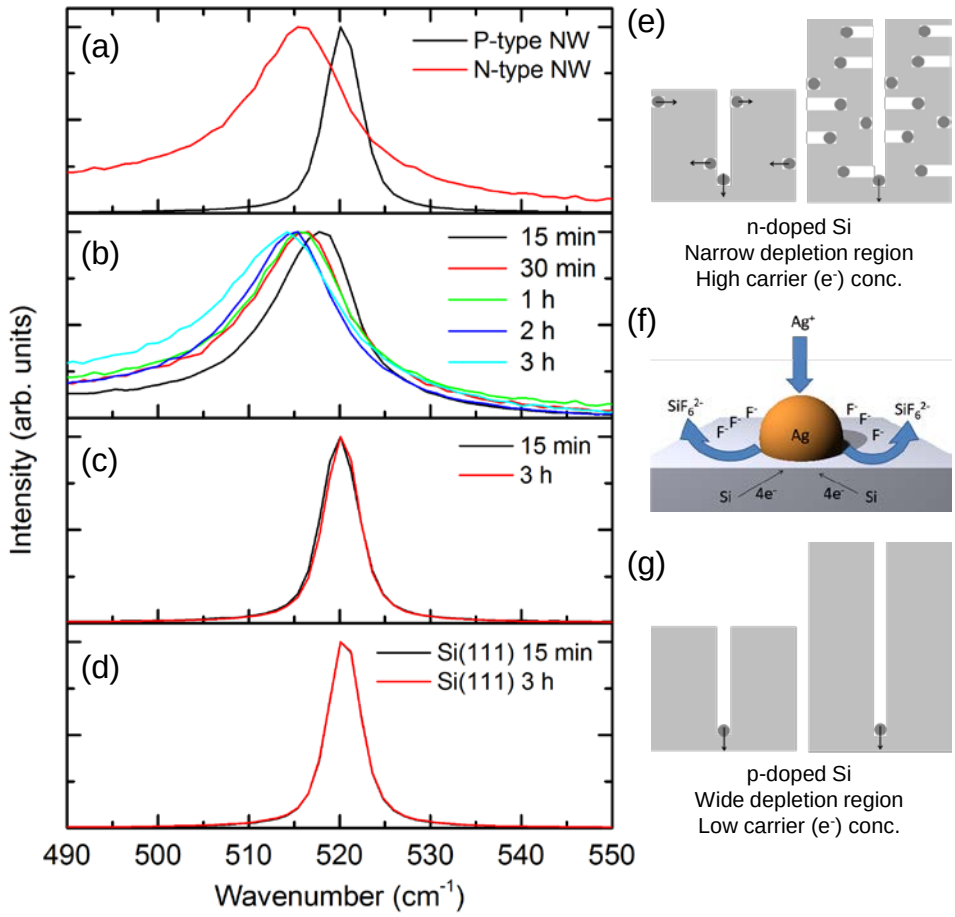

Figure 3. (a) Raman spectra of n^+-NWs and p-NWs etched for one hour (b) Raman spectra of n^+-NWs that were etched for varying lengths of time. (c) Raman spectra of p-NWs that were etched for 15 mins and 3 hours and (d) Raman spectra for NWs from n-Si(111) etched for 15 mins and 3 hours. (e) Schematic of the etching mechanism of highly doped Si. (f) Schematic of Ag particles deposited on Si substrate. (g) Schematic of etching mechanism of low doped Si.

The redshift and broadening of the TO phonon mode is not observed for the p-NWs (Fig. 3(c)) nor the n-NWs formed from the Si(111) wafer (Fig. 3(d)). Further work is needed to clarify if a high carrier concentration under reverse bias initiates a reverse tunneling

mechanism that allows etching limited by the depletion region (Fig. 3(g)). This mechanism is well established in electrochemical etching protocols for porous silicon for example.

To verify that the n^+-NWs become more internally mesoporous with etching time compared to p-NWs that exhibit surface roughening of smaller NWs, we examined the Si NWs by TEM. Figure 4 shows the n^+-NWs etched for 15 mins (a,b), 1 h (c,d) and 3 h (e,f). The images indicate that the NWs themselves become more mesoporous with etching time, and porosity develops from the outer surface initially (Fig. 4(a)). The inset to Fig. 4(f) shows a HRTEM image of the edge region of a typical mesoporous n^+-NW and shows the network of nanocrystal that comprises the skeletal structure of the NWs.

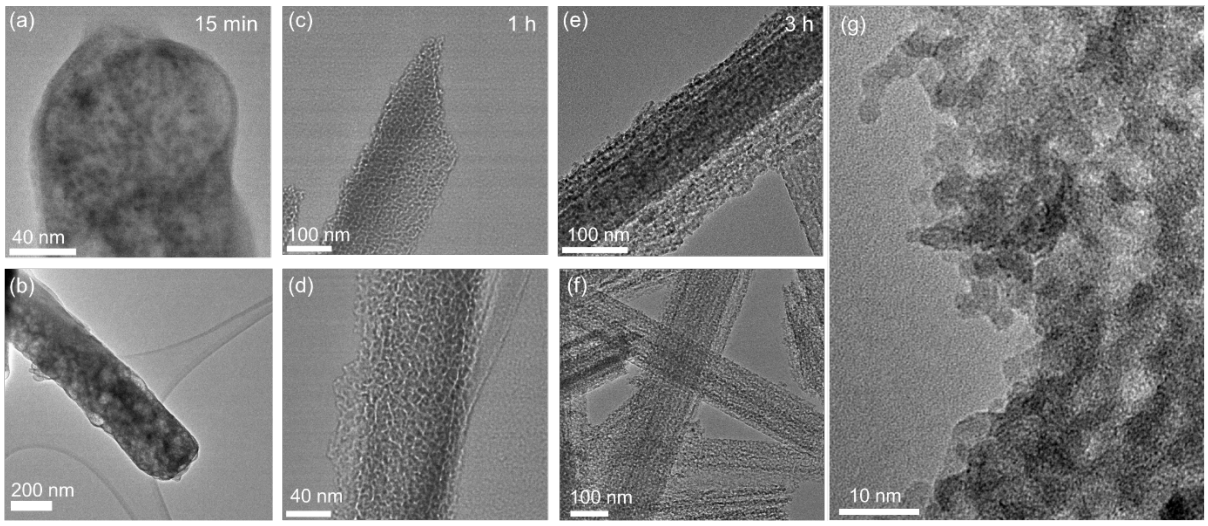

Figure 4. TEM images of n^+-NWs etched for 15 mins (a,d), 1 hour (b,e) and 3 hours (c,f). (g) HRTEM image of the edge region of a typical mesoporous NW showing the network of nanocrystalline silicon.

In p-Si in Fig. 5, the higher hole concentration at the surface under accumulation mode because of a forward bias electrochemical condition, facilitates thinning of the overall wire rather than site selective etching of the sidewalls. Such a process would leave rough walls and narrower wires, but no internal porosity under the same etching conditions[67], which agrees with observation. Figures 5(a) and (c) show the p-NWs etched for 15 mins and 3 h respectively, while NWs from n-Si(111) wafers etched for similar duration are shown in Figs 5(b) and (d).

The p-NWs are never found to develop internal mesoporosity with increasing etching time. An electron diffraction pattern of a NW etched from the Si(111) wafer is an inset in Fig. 5(b) confirming the [100] orientation nature of the smooth-surfaced NW. NW lattice planes as etched from a (111) substrate are measured to be at 51.7° to the <100> directions.

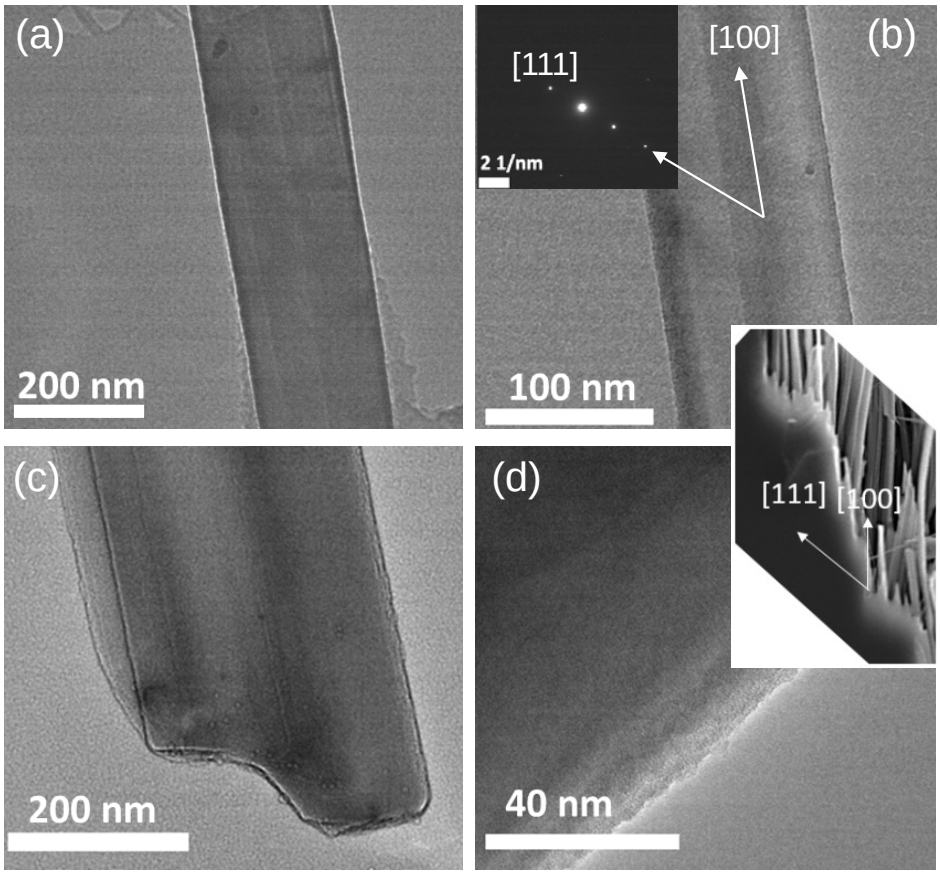

Figure 5. TEM images of (a) p-NWs etched for 15 mins (b) NWs etched from Si(111) for 15 mins (c) p-NWs etched for 3 hours and (d) NWs etched from Si(111) for 3 hours. (Inset) SEM image of NWs etched from a n-Si(111) wafer showing the [100] orientation of the NWs.

Phonon scattering and NW mesoporosity – Effect of Temperature, $AgNO_3$ and HF concentration

Silver nanoparticles can disintegrate and redeposit on the sidewalls of Si NWs resulting in porous Si NWs. The development of mesoporosity in MAC etching of Si NWs was examined at higher temperatures to examine the effect of thermal excitation that promotes electron

transfer on the etching[31, 38, 42, 53]. Figure 6(a) shows the TO phonon mode response of n^+-Si NWs that were etched at 25-75 ºC, respectively and multi-phonon confinement processes (a peak shift and asymmetric broadening) are found, indicative of mesoporosity development. TEM images in Figs 7(a) and (b) confirm Si NWs etched at 25 and 75 ºC develop and retain internal mesoporosity. A better degree of consistent mesoporosity is found at the higher temperature (Fig. 7(b), with other conditions constant.

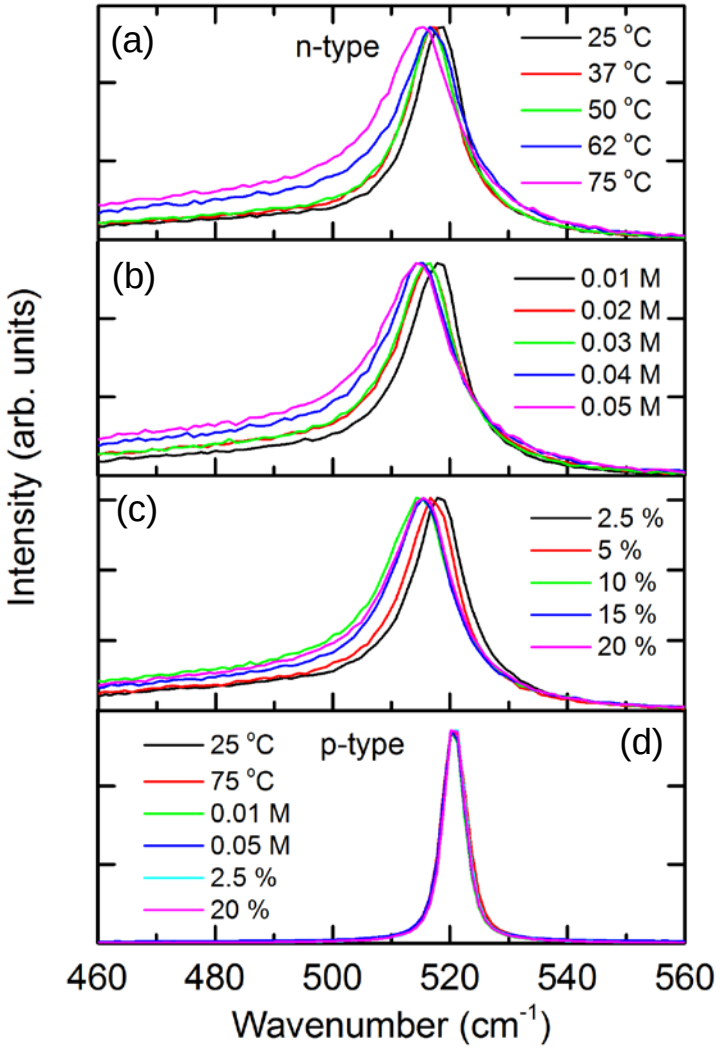

Figure 6. (a) Raman spectra of n^+-Si(100) NWs etched at various temperatures. (b) Raman spectra from n^+-Si NWs etched with various $AgNO_3$ concentrations. (c) Raman spectra of n^+-Si NWs etched with different HF concentrations. (d) Raman spectra of p-NWs etched under both extremes of each etching condition in (a-c).

The $AgNO_3$ concentration was varied between 0.01 M and 0.05 M to examine the influence of a higher concentration of Ag^+ ions (or there reduction, re-oxidation and re-

deposition on the NW surface) may influence the formation of internal mesoporosity in n^+, n and p-Si.[31, 42]. For n^+-Si NWs that become mesoporous, a higher [Ag^+] resulted in a red shift and asymmetric broadening of the TO phonon mode, as shown in Raman spectra in Fig. 6(b), consistent with a reduction in Si nanocrystallite size within the mesoporous structure. TEM analysis (Figs. 7(c) and (d)) confirms the increase in porosity within NWs at greater $AgNO_3$ concentration up to 0.05 M.

Unlike the development of mesoporosity in n^+-Si NWs via increases in Ag concentration and temperature, the %HF variation (from 2.5 to 20%) results in an increase is mesoporosity (reduction in average Si crystallite size within the NWs) up to 15% HF, as shown in Fig. 7(c). The Raman shift of the TO phonon mode confirms increasing porosity, but also highlights that 20% HF does not appreciably alter the degree of porosity beyond that found for 2.5-15% HF. TEM examination in Fig. 7(e) and (f) shows porous NWs with slightly rougher overall morphology, which tends toward greater mesoporosity throughout as the NW reaches the limit of internal mesoporosity. NWs formed at 20% HF (Fig. 7(f)) are semi-transparent to the 200 kV electron beam and typically. No redshift nor asymmetric broadening from quantum confinement effects or internal boundary phonon scattering are found for p-NWs for any of the etching conditions (Fig. S2, Supporting Information).

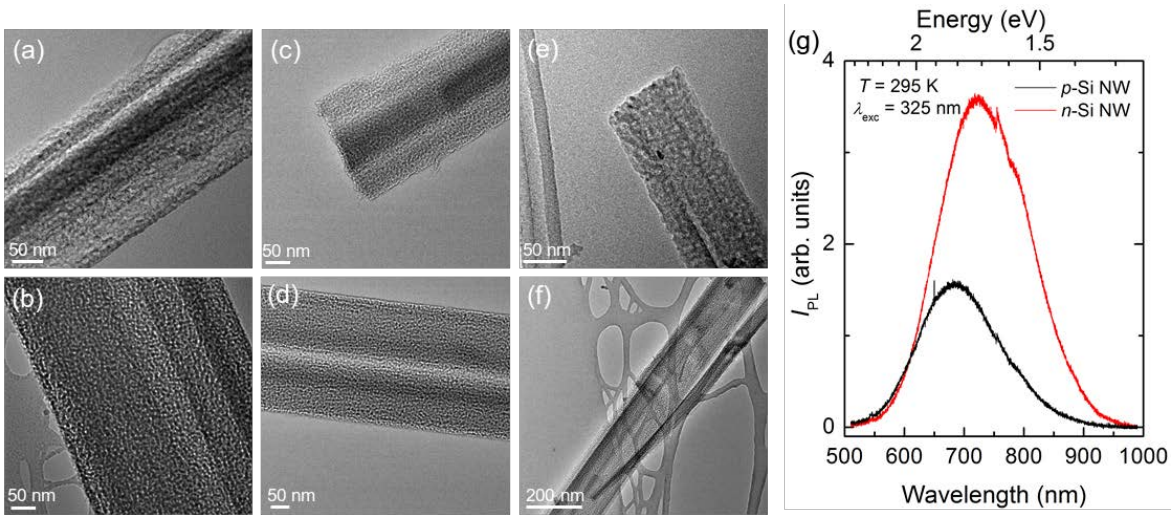

Figure 7. TEM images of n^+-NWs etched at (a) 25 ºC and (b) 75 ºC; (c) 0.01 M and (d) 0.05 M $AgNO_3$; and (e) 2.5% HF and (f) 20% HF. (g) PL spectra acquired at room temperature from p-NWs and n^+-NWs.

Si NWs, porous silicon and some silicon nanoparticle systems have been shown to be efficient light emitters at room temperature, with intense red light from confined photons [72-74]. The procedures here for induced internal mesoporosity into the Si NWs are very effective at producing a high density of nanocrystallites with dimensions less than the Bohr radius in an internal random network arrangement. At room temperature, there is negligible recombination of photo-generated carriers from electron-phonon coupling, yet as seen in Fig. 7, we observe intense red light emission from the mesoporous NW layers. Figure 7 shows PL spectra from rough p- and mesoporous n^+-Si NWs obtained by exciting with the 325 nm line of a HeCd cw laser. The PL emission is centered at about 720 nm for n^+-Si NWs with internally mesoporous structure, and at ~685 nm for p-NWs that are <100 nm in diameter with a high density of small surface crystallites on the rough surface. While quantum confinement effects are responsible for the observed light emission, the higher emission energy for rough, solid p-NW is from smaller surface roughness asperities that have much lower intensity compared to the red emission from n^+-Si NWs. The emission for n^+- mesoporous NWs is very bright red and clearly visible with the naked eye, but emission from the p-NW is very weak and invisible to the naked eye.

The experimental conditions that lead to electroless etching conditions for highly mesoporous Si NWs have been shown to directly affect the formation of internal mesoporosity. These mesoporous NWs and the etching conditions that affect their structure are also amenable to analysis by Raman scattering by thermalizing phonons directly using high laser powers. As quantum confinements and phonon scattering effects lead to reduced thermal conductivity, direct focused laser heating of NW bundles can relate the degree of mesoporosity formed from

each experimental etching condition to the nanoscale structure by probing variations in effective thermal diffusivity. Pristine but labyrinthine arrangement of unetched Si comprising the mesoporous internal structure as reported here may be sufficient to reduced phonon transport; each are governed by specifically different Raman scattering responses that may or may not include size effects [77].

The laser power was varied for the n^+-NWs that were etched for (a) 15 mins, (b) 1 h and (c) 3 h shown in Fig. 8, corresponding to localized heating of the NWs. From Fig. 8(c) the highly porous wires cause a greater Raman redshift and a broadening than less porous wires in Fig. 8(a+b). The shift and broadening of the n^+-Si NW Raman peaks is due to anharmonic effects as a result of thermally excited lattice phonons that are both confined and scattered in the networked mesoporous NW structure. [76] The highly porous Si NWs do not dissipate heat efficiently due to a reduced thermal conductivity. Mesoporous n^+-NWs, as shown in Fig. 8, exhibit the greatest shift in TO phonon scattering with increased temperature consistent with multi-phonon processes from an optimum degree of internal mesoporosity is reached.

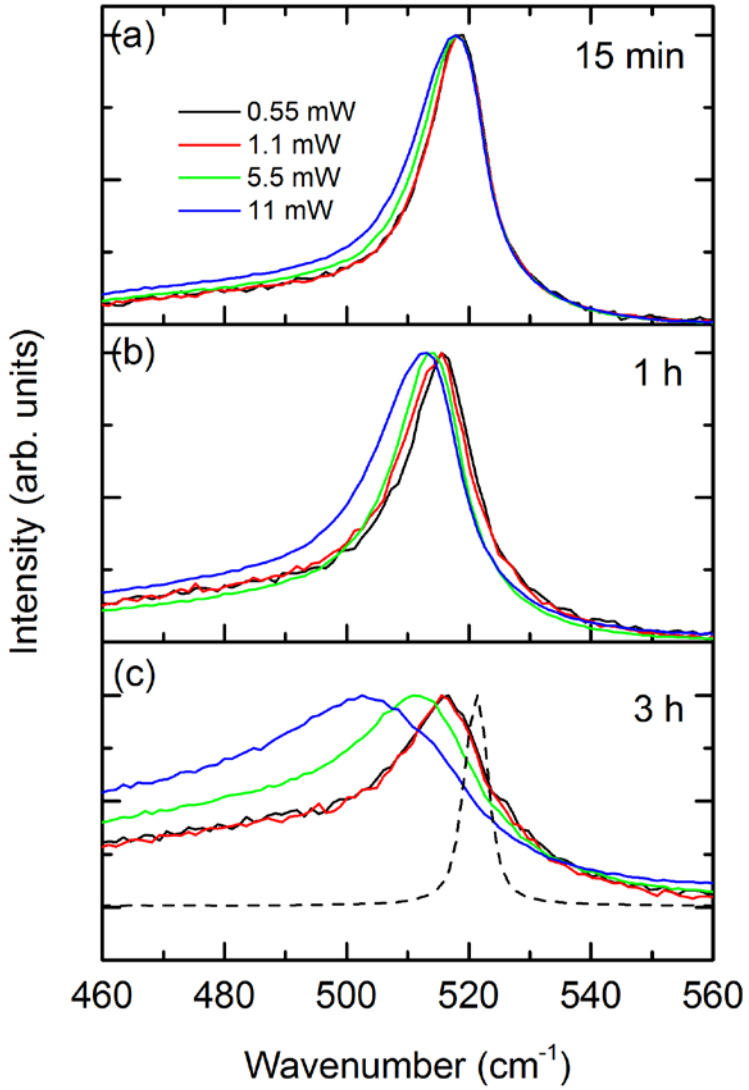

Figure 8. Raman spectra for n^+-NWs etched for (a) 15 mins (b) 1 h and (c) 3 h and heated at various laser powers. A Raman scattering spectrum of a bulk Si wafer (black dashed curve) is shown for reference.

Non-porous Si NWs produced from highly doped n^+-Si

It is now known that highly doped n^+-Si produces mesoporous Si NWs under many etching conditions, as demonstrated earlier. Next, we show how non-porous Si NWs can be formed within the NW layer from a highly doped Si wafer, i.e. secondary intra-NW etching is prevented during NW layer formation. We etched the highly doped n^+-Si(100) used in this study using the following "low" etching conditions: 2.5 % HF, 0.01 M $AgNO_3$, at 25 ºC for 15 mins. What resulted were extremely short Si NWs as shown in the SEM image in Fig. 9(a). The Si NWs are ~500 nm in length and are so short and rigid (no internal porosity) that

clumping observed during drying for longer, less rigid NWs does not influence the Si NWs layer uniformity. The Raman scattering data in shown in Fig. 9(c) indicates that the Si NWs are non-porous and the TO phonon remains similar to that of bulk Si. This is verified by the TEM images in Figs 9 (c) and (c), where predominantly crystalline silicon is observed with minimal surface roughness. An electron diffraction pattern in Fig. 9 (e) shows the quasi-polycrystalline nature of the Si NWs superimposed with arcing of the diffraction spots from rotated crystallites within the NW structure. The data demonstrate that Si NWs formed from highly doped Si begin as single crystalline NWs and the more gentle etching conditions result in the development of surface inhomogeneities and some degree of internal modification to the crystal structure. The NW remain solid and eventually become porous during etching if etching conditions as defined in this work are modified. The initiation of porosity by the formation of thinner regions within the NWs is believed to allow rotation of crystalline regions that contributes to a degree of multi-axial nanocrystalline texture. Multiple lattice fringes or oriented crystallites comprising the rough outer surface of the NWs can also be seen in Fig. 9 (d).

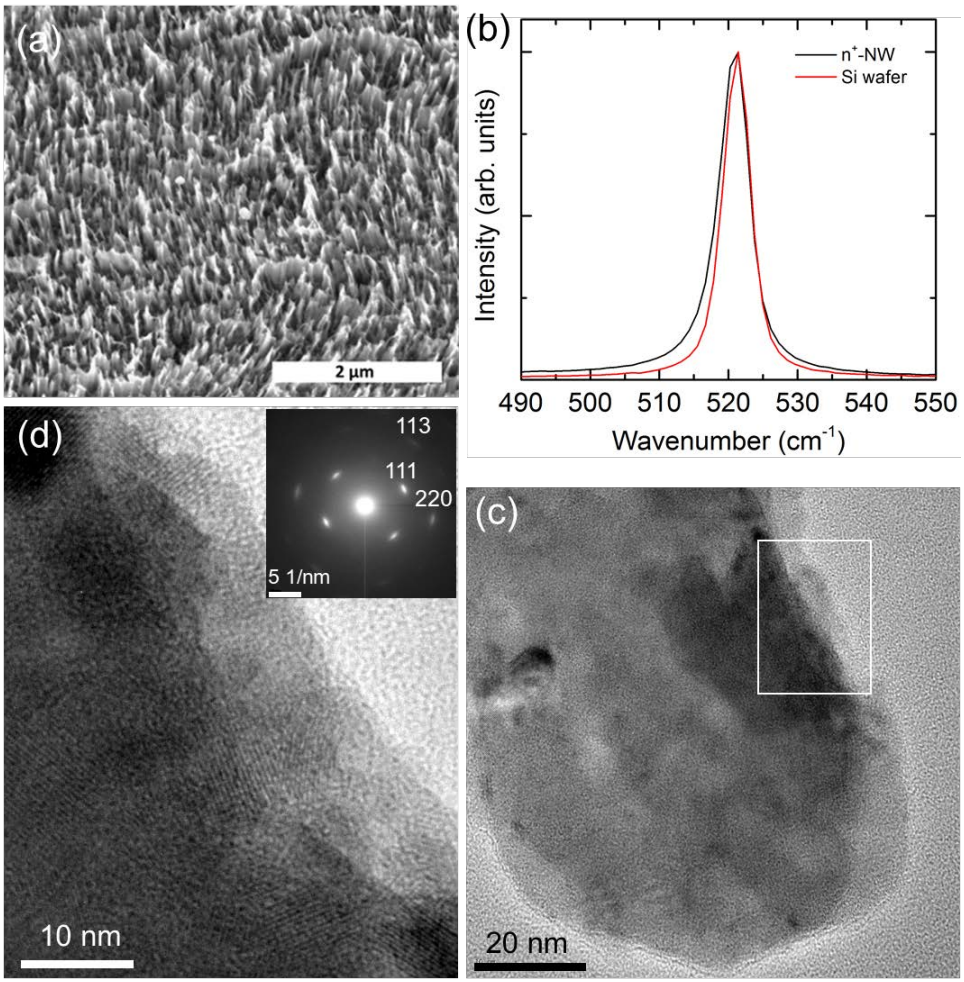

Figure 9. (a) SEM image of the n^+-Si NW layer. (b) Raman spectra of the n^+-NWs and of bulk Si wafer. (c) TEM image of a non-porous n^+-Si NW and (d) HRTEM and electron diffraction pattern of the non-porous, polycrystalline n^+-Si NWs formed under the "low" etching conditions.

Porous Si produced from low doped p-type Si

Porous p-type NWs were also produced from the low carrier concentration p-Si(100) wafers used in this study. Etching under "high" etching conditions, namely 0.1 M $AgNO_3$, 20% HF, for 3h at 63 ºC were used. The porous nature of the NWs, similar to n^+-NWs, caused a redshift and broadening of the TO phonon mode (Fig. 10(a)). The NWs produced within the layer (Fig. 10(a)) were internally mesoporous in nature as shown in the TEM image of a single NW in Fig. 10(c) and (d), where regions of underdeveloped mesoporosity is characteristic. It should

be noted that that mesoporosity in p-type NWs was not attainable when any one of the etching parameters was reduced.

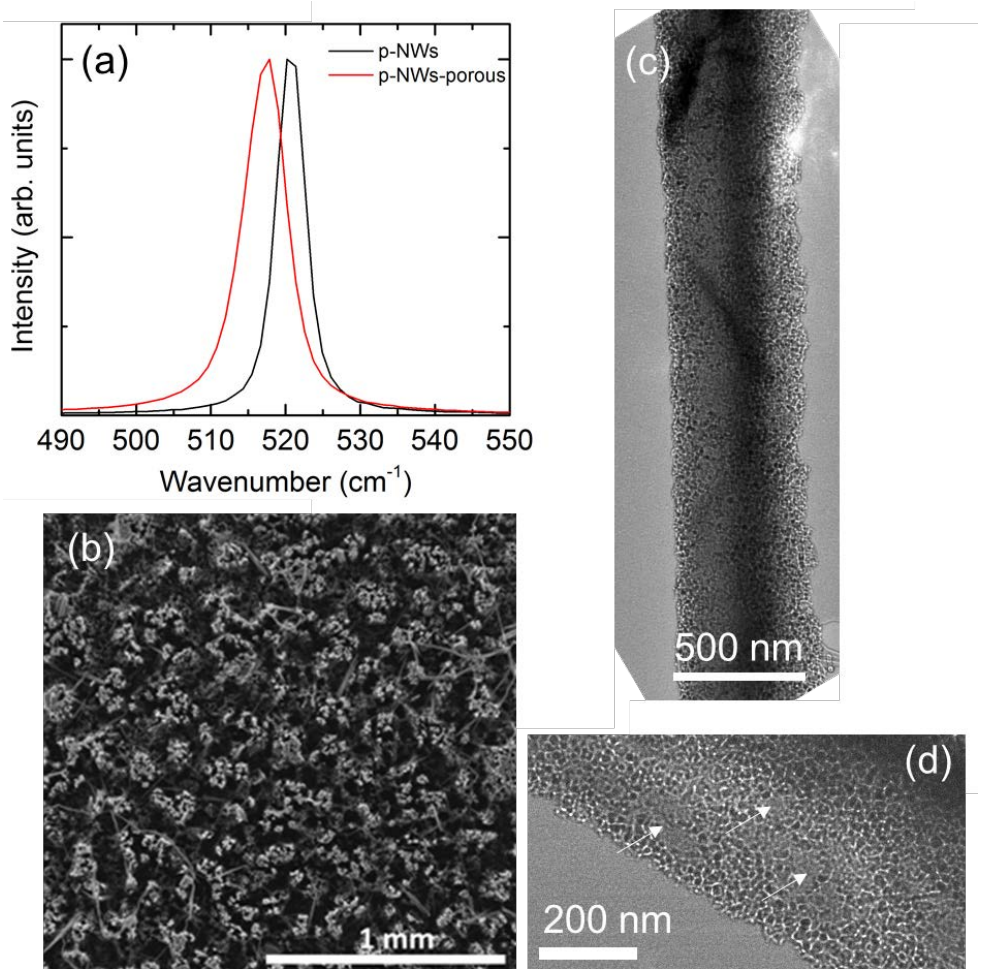

Figure 10. (a) Raman spectra of p-NWs under normal etching condition and under the "high" etching conditions under which internal mesoporosity develops. (b) Plan-view SEM image of the NW layer. (c) TEM image of a single mesoporous p-NW and (d) TEM image showing regions of underdeveloped internal porosity within the mesoporous p-NW.

Overall, the variation is Raman phonon mode shape is not found to be consistent with stress-induced changes, as mesoporous crystal are inherently lower stress condition that bulk silicon. Nonetheless, the relationship between the phonon mode shift, peak shape, and crystallite size reported here for mesoporous provide a useful means for using Raman scattering as a tool to measure size and the etching mode in a range of semiconductor systems. The ability to tune the etching conditions for different Si conduction types and wafers, to form black silicon

made from arrays of internally mesoporous Si NWs may be useful for Li-ion batteries, light emission and absorption, sensors and other systems that rely on electrochemical, optical or thermal characteristics that are affected by internal crystal structure and size.

IV. Conclusions

Silicon etched in a HF and $AgNO_3$ containing solutions for various times form layers of mesoporous and rough NWs, respectively from a MACE process. Our results show how the change in wafer conductivity affects the nature of the NW layer formed during etching. As selectively etched NW layers, p-Si(100) etches at a higher rate than n^+-Si, but does not develop internal mesoporosity under standard etching conditions. The influence of a range of etching conditions were examined in detail, including variations in $AgNO_3$ concentration, HF concentration and etching temperature. The Raman scattering spectra for each condition was characterized by a TO phonon mode a peak redshift and asymmetric broadening when etching parameters were increased (increase in porosity). TEM analysis confirmed a mesoporous Si structure in n^+ Si NWs which are made up of a random internal network of nanoscale crystallites of silicon, as a mesoporous NW.

The development of mesoporosity as a function of etching conditions are monitored by changes in phonon transport and scattering mechanisms by Raman scattering measurements, and confirmed through detailed electron microscopy. Direct laser heating during Raman scattering measurements shows that the increasingly mesoporous Si NWs contribute to a greater shift in the transverse optical phonon and increased FWHM of this mode when compared to the less porous Si NWs, because of a reduced thermal conductivity and confinement of acoustic phonons. Non porous Si NWs are also produced from highly doped Si under a specific etching protocol, so that conductive solid-core n^+-NWs are formed. n-Si(111)

also relieved NWs oriented along preferential <100> directions, in three distinct orientations and do not develop internal mesoporosity.

This hierarchical porosity is characterized by increased NW surface roughness, a high degree of internal boundary scatterers, and a carrier depleted mesoporous skeleton. The response is characteristic of surface scattering and multi-phonon processes including confinement. The formation of such small internal structure, in the absence of stress-related effects and Si-OSi and similar species, is likely necessary to explain the shift in the TO phonon modes often reported from NW diameter reduction. These factors are ideal for phonon scattering and reducing the thermal conductivity for Si NW based thermoelectric and thermal interface materials, and for producing electrochemically in active (or inactive when full porous) high surface area materials for pseudocapacitor or Li-ion battery applications.

Acknowledgments

WMS acknowledges support under the framework of the INSPIRE programme, funded by the Irish Government's Programme for Research in Third Level Institutions, Cycle 4, National Development Plan 2007-2013. CG acknowledges financial support from the Irish Research Council under Award No. RS/2011/797. COD acknowledges support from Science Foundation Ireland under Award no. 07/SK/B1232a. This research has received funding from the Seventh Framework Programme FP7/2007-2013 (Project STABLE) under grant agreement n°314508. This work was also supported by SFI under the National Access Programme (NAP 417). The authors acknowledge useful and informative comments from one of the reviewers.

References

[1] Geyer N, Huang Z, Fuhrmann B, Grimm S, Reiche M, Nguyen-Duc T-K, Boor J d, Leipner H S, Werner P and Gosele U 2009 *Nano Lett.* **9** 3106

[2] McDowell M T, Lee S W, Nix W D and Cui Y 2013 25th Anniversary Article: Understanding the Lithiation of Silicon and Other Alloying Anodes for Lithium‐Ion Batteries *Advanced Materials* **25** 4966-85
[3] McSweeney W, Geaney H and O'Dwyer C 2015 Metal assisted chemical etching of silicon and the behaviour of nanoscale silicon materials as Li-ion battery anodes *Nano Res.*
[4] Chan C K, Peng H, Liu G, McIlwrath K, Zhang X F, Huggins R A and Cui Y 2008 High-performance lithium battery anodes using silicon nanowires *Nature Nanotechnology* **3** 31-5
[5] Osiak M, Geaney H, Armstrong E and O'Dwyer C 2014 Structuring materials for lithium-ion batteries: advancements in nanomaterial structure, composition, and defined assembly on cell performance *Journal of Materials Chemistry A* **2** 9433-60
[6] Armstrong M J, O'Dwyer C, Macklin W J and Holmes J D 2014 Evaluating the performance of nanostructured materials as lithium-ion battery electrodes *Nano Research* **7** 1-62
[7] McSweeney W, Lotty O, Glynn C, Geaney H, Holmes J D and O'Dwyer C 2014 The influence of carrier density and doping type on lithium insertion and extraction processes at silicon surfaces *Electrochim. Acta* **135** 356–67
[8] Quiroga-González E, Ossei-Wusu E, Carstensen J and Föll H 2011 How to make optimized arrays of Si wires suitable as superior anode for Li-ion batteries *J. Electrochem. Soc.* **158** E119-E23
[9] Föll H, Carstensen J, Ossei-Wusu E, Cojocaru A, Quiroga-González E and Neumann G Optimized Cu-Contacted Si Nanowire Anodes for Li Ion Batteries Made in a Production Near Process *J. Electrochem. Soc.* **158** A580-A4
[10] Quiroga-González E, Carstensen J and Föll H 2013 Good cycling performance of high-density arrays of Si microwires as anodes for Li ion batteries *Electrochim. Acta* **101** 93–8
[11] Boukai A I, Bunimovich Y, Tahir-Kheli J, Yu J-K, Goddard Iii W A and Heath J R 2008 Silicon nanowires as efficient thermoelectric materials *Nature* **451** 168-71
[12] Hochbaum A I, Chen R, Delgado R D, Liang W, Garnett E C, Najarian M, Majumdar A and Yang P 2008 Enhanced thermoelectric performance of rough silicon nanowires *Nature* **451** 163-7
[13] Kelzenberg M D, Turner-Evans D B, Kayes B M, Filler M A, Putnam M C, Lewis N S and Atwater H A 2008 Photovoltaic measurements in single-nanowire silicon solar cells *Nano letters* **8** 710-4
[14] Föll H, Langa S, Carstensen J, Christophersen M and Tiginyanu I M 2003 Pores in III–V semiconductors *Advanced Materials* **15** 183
[15] O'Dwyer C, Buckley D N, Sutton D, Serantoni M and Newcomb S B 2007 An Investigation by TEM and AFM of the Mechanism of Anodic Formation of Nanoporosity in n-InP in KOH *J. Electrochem. Soc.* **154** H78-H85
[16] O'Dwyer C, Buckley D N, Sutton D and Newcomb S B 2006 Anodic Formation and Characterization of Nanoporous InP in Aqueous KOH Electrolytes *J. Electrochem. Soc.* **153** G1039-G46
[17] Lynch R P, Quill N, O'Dwyer C, Nakahara S and Buckley D N 2013 Propagation of Nanopores During Anodic Etching of n-InP in KOH *Phys. Chem. Chem. Phys.* **15** 15135-45
[18] Lynch R, O'Dwyer C, Sutton D, Newcomb S B and Buckley D N 2007 Nanoporous Domains in n-InP Anodized in KOH *ECS Trans.* **6** 355-66

[19] Lynch R, O'Dwyer C, Quill N, Nakahara S, Newcomb S B and Buckley D N 2013 Pore Propagation Directions and Nanoporous Domain Shape in n-InP Anodized in KOH *J. Electrochem. Soc.* **160** D260-D70
[20] Gerngross M-D 2012 Single-Crystalline Membranes in Indium Phosphide: Fabrication Process and Characterization Using FFT Impedance Analysis *Journal of The Electrochemical Society* **159** H857
[21] Santinacci L, Gonçalves A M, David C, Eb A, Gerard I, Mathieu C, Herlem M and Etcheberry A 2007 In situ electrochemical characterization of porous n -InP (100) *physica status solidi (c)* **4** 1898-902
[22] Santinacci L, Bouttemy M, Gerard I and Etcheberry A 2009 Unexpected Dissolution Process at Porous n-InP Electrodes *ECS Transactions* **19** 313-9
[23] Eb A, Gonçalves A M, Mathieu C and Etcheberry A 2008 Growth of a Porous Layer on InP in Liquid Ammonia: A Specific Interfacial Behavior *ECS Transactions* **16** 417-24
[24] Lotty O, Petkov N, Georgiev Y M and Holmes J D 2012 Porous to Nonporous Transition in the Morphology of Metal Assisted Etched Silicon Nanowires *Jpn. J. Appl. Phys.* **51** 11PE03-1
[25] Geyer N, Huang Z, Fuhrmann B, Grimm S, Reiche M, Nguyen-Duc T-K, de Boor J, Leipner H S, Werner P and Gösele U 2009 Sub-20 nm Si/Ge superlattice nanowires by metal-assisted etching *Nano letters* **9** 3106-10
[26] Lee D H, Kim Y, Doerk G S, Laboriante I and Maboudian R 2011 Strategies for controlling Si nanowire formation during Au-assisted electroless etching *Journal of Materials Chemistry* **21** 10359-63
[27] Beale M I J, Benjamin J D, Uren M J, Chew N G and Cullis A G 1985 An experimental and theoretical study of the formation and microstructure of porous silicon. *J. Cryst. Growth* **73** 622
[28] Lehman V 2002 *Electrochemistry of Silicon* (Weinheim, Germany: Wiley-VCH)
[29] Smith R L and Collins S D 1992 Porous silicon formation mechanisms. *J. Appl. Phys.* **71** R1
[30] Hochbaum A I, Gargas D, Hwang Y J and Yang P 2009 Single Crystalline Mesoporous Silicon Nanowires *Nano Letters* **9** 3550-4
[31] Zhang M-L, Peng K-Q, Fan X, Jie J-S, Zhang R-Q, Lee S-T and Wong N-B 2008 Preparation of Large-Area Uniform Silicon Nanowires Arrays through Metal-Assisted Chemical Etching *The Journal of Physical Chemistry C* **112** 4444-50
[32] Hochbaum A I, Gargas D, Hwang Y J and Yang P 2009 Single Crystalline Mesoporous Silicon Nanowires *Nano Lett.* **9** 3550
[33] Zhong X, Qu Y, Lin Y-C, Liao L and Duan X 2011 Unveiling the Formation Pathway of Single Crystalline Porous Silicon Nanowires *ACS Appl. Mater. Interfaces* **3** 261
[34] Ghossoub M G, Valavala K V, Seong M, Azeredo B, Hsu K, Sadhu J S, Singh P K and Sinha S 2013 Spectral Phonon Scattering from Sub-10 nm Surface Roughness Wavelengths in Metal-Assisted Chemically Etched Si Nanowires *Nano Lett.* **13** 1564
[35] Lim J, Hippalgaonkar K, Andrews S C, Majumdar A and Yang P 2012 Quantifying Surface Roughness Effects on Phonon Transport in Silicon Nanowires *Nano Lett.* **12** 2475
[36] Hochbaum A I, Chen R K, Delgado R D, Liang W J, Garnett E C, Najarian M, Majumdar A and Yang P D 2008 Enhanced thermoelectric performance of rough silicon nanowires. *Nature* **451** 163
[37] Qu Y, Liao L, Li Y, Zhang H, Huang Y and Duan X 2009 Electrically conductive and optically active porous silicon nanowires *Nano letters* **9** 4539-43

[38] Chern W, Hsu K, Chun I S, Azeredo B P d, Ahmed N, Kim K-H, Zuo J-m, Fang N, Ferreira P and Li X 2010 Nonlithographic Patterning and Metal-Assisted Chemical Etching for Manufacturing of Tunable Light-Emitting Silicon Nanowire Arrays *Nano Letters* **10** 1582-8
[39] Chartier C, Bastide S and Lévy-Clément C 2008 Metal-assisted chemical etching of silicon in HF–H_2O_2 *Electrochimica Acta* **53** 5509-16
[40] Geyer N, Fuhrmann B, Huang Z, de Boor J, Leipner H S and Werner P 2012 Model for the Mass Transport during Metal-Assisted Chemical Etching with Contiguous Metal Films As Catalysts *J. Phys. Chem. C* **116** 13446
[41] Bang B M, Kim H, Song H-K, Cho J and Park S 2011 Scalable approach to multi-dimensional bulk Si anodes via metal-assisted chemical etching *Energy & Environmental Science* **4** 5013-9
[42] Zhong X, Qu Y, Lin Y-C, Liao L and Duan X 2011 Unveiling the Formation Pathway of Single Crystalline Porous Silicon Nanowires *ACS Appl. Mater. Interfaces* **3** 261-70
[43] Fang H, Li X, Song S, Xu Y and Zhu J 2008 Fabrication of slantingly-aligned silicon nanowire arrays for solar cell applications *Nanotechnology* **19** 255703
[44] Goldberger J, Hochbaum A I, Fan R and Yang P 2006 Silicon Vertically Integrated Nanowire Field Effect Transistors *Nano Letters* **6** 973-7
[45] Schmidt V, Riel H, Senz S, Karg S, Riess W and Gösele U 2006 Realization of a Silicon Nanowire Vertical Surround-Gate Field-Effect Transistor *Small* **2** 85-8
[46] Peng K, Fang H, Hu J, Wu Y, Zhu J, Yan Y and Lee S 2006 Metal-particle-induced, highly localized site-specific etching of Si and formation of single-crystalline Si nanowires in aqueous fluoride solution *Chemistry-a European Journal* **12** 7942-7
[47] Peng K Q, Wu Y, Fang H, Zhong X Y, Xu Y and Zhu J 2005 Uniform, axial-orientation alignment of one-dimensional single-crystal silicon nanostructure arrays *Angewandte Chemie-International Edition* **44** 2737-42
[48] Chen C Y, Wu C S, Chou C J and Yen T J 2008 Morphological Control of Single‐Crystalline Silicon Nanowire Arrays near Room Temperature *Advanced Materials* **20** 3811-5
[49] Peng K, Lu A, Zhang R and Lee S T 2008 Motility of metal nanoparticles in silicon and induced anisotropic silicon etching *Advanced Functional Materials* **18** 3026-35
[50] Peng K, Zhang M, Lu A, Wong N-B, Zhang R and Lee S-T 2007 Ordered silicon nanowire arrays via nanosphere lithography and metal-induced etching *Applied physics letters* **90** 163123--3
[51] Huang Z, Shimizu T, Senz S, Zhang Z, Geyer N and Gösele U 2010 Oxidation rate effect on the direction of metal-assisted chemical and electrochemical etching of silicon *The Journal of Physical Chemistry C* **114** 10683-90
[52] Tsujino K and Matsumura M 2007 Morphology of nanoholes formed in silicon by wet etching in solutions containing HF and H2O2 at different concentrations using silver nanoparticles as catalysts *Electrochimica Acta* **53** 28-34
[53] Kim J, Han H, Kim Y H, Choi S-H, Kim J-C and Lee W 2011 Au/Ag Bilayered Metal Mesh as a Si Etching Catalyst for Controlled Fabrication of Si Nanowires *ACS Nano* **5** 3222-9
[54] Tian B, Xie P, Kempa T J, Bell D C and Lieber C M 2009 Single-crystalline kinked semiconductor nanowire superstructures *Nature nanotechnology* **4** 824-9
[55] Adu K, Xiong Q, Gutierrez H, Chen G and Eklund P 2006 Raman scattering as a probe of phonon confinement and surface optical modes in semiconducting nanowires *Applied Physics A* **85** 287-97
[56] Ponomareva I, Srivastava D and Menon M 2007 Thermal conductivity in thin silicon nanowires: phonon confinement effect *Nano letters* **7** 1155-9

[57] Balkanski M, Wallis R and Haro E 1983 Anharmonic effects in light scattering due to optical phonons in silicon *Physical review. B, Condensed matter* **28** 1928-34
[58] Wang R-p, Zhou G-w, Liu Y-l, Pan S-h, Zhang H-z, Yu D-p and Zhang Z 2000 Raman spectral study of silicon nanowires: High-order scattering and phonon confinement effects *Physical Review B* **61** 16827-32
[59] Wang Z, Ni Z, Zhao R, Chen M, Bi K and Chen Y 2011 The effect of surface roughness on lattice thermal conductivity of silicon nanowires *Physica B: Condensed Matter* **406** 2515-20
[60] Carrete J, Gallego L J, Varela L M and Mingo N 2011 Surface roughness and thermal conductivity of semiconductor nanowires: Going below the Casimir limit *Physical Review B* **84** 075403
[61] Meng C-Y, Chen J-L, Lee S-C and Chia C-T 2006 Doping effects on the Raman spectra of silicon nanowires *Physical Review B* **73** 245309
[62] Balasundaram K, Sadhu J S, Shin J C, Azeredo B, Chanda D, Malik M, Hsu K, Rogers J A, Ferreira P, Sinha S and Li X 2012 Porosity control in metal assisted chemical etching of degenerately doped silicon *Nanotechnology* **23** 305304
[63] Lynch R P, O'Dwyer C, Quill N, Nakahara S, Newcomb S B and Buckley D N 2013 Pore Propagation Directions and Nanoporous Domain Shape in n-InP Anodized in KOH *Journal of The Electrochemical Society* **160** D260-D70
[64] Lee C-L, Tsujino K, Kanda Y, Ikeda S and Matsumura M 2008 Pore formation in silicon by wet etching using micrometre-sized metal particles as catalysts *Journal of Materials Chemistry* **18** 1015-20
[65] Zhang M-L, Peng K-Q, Fan X, Jie J-S, Zhang R-Q, Lee S-T and Wong N-B 2008 Preparation of large-area uniform silicon nanowires arrays through metal-assisted chemical etching *Journal of Physical Chemistry C* **112** 4444-50
[66] Bai F, To W-K and Huang Z 2013 Porosification-Induced Back-Bond Weakening in Chemical Etching of n-Si(111) *The Journal of Physical Chemistry C* **117** 2203-9
[67] McSweeney W, Lotty O, Mogili N, Glynn C, Geaney H, Tanner D, Holmes J and O'Dwyer C 2013 Doping controlled roughness and defined mesoporosity in chemically etched silicon nanowires with tunable conductivity *Journal of Applied Physics* **114** 034309
[68] Quiroga-González E, Carstensen J, Glynn C, O'Dwyer C and Föll H 2014 Pore size modulation in electrochemically etched macroporous p-type silicon monitored by FFT impedance spectroscopy and Raman scattering *Physical Chemistry Chemical Physics* **16** 255-63
[69] Lynch R P, Quill N, O'Dwyer C, Nakahara S and Buckley D N 2013 Propagation of nanopores during anodic etching of n-InP in KOH *Phys. Chem. Chem. Phys.* **15** 15135-45
[70] Kiraly B, Yang S and Huang T J 2013 Multifunctional porous silicon nanopillar arrays: antireflection, superhydrophobicity, photoluminescence, and surface-enhanced Raman scattering *Nanotechnology* **24** 245704
[71] Viera G, Huet S and Boufendi L 2001 Crystal size and temperature measurements in nanostructured silicon using Raman spectroscopy *Journal of Applied Physics* **90** 4175-83
[72] Zi J, Büscher H, Falter C, Ludwig W, Zhang K and Xie X 1996 Raman shifts in Si nanocrystals *Applied Physics Letters* **69** 200-2
[73] Chen W, Fan Z, Dhanabalan A, Chen C and Wang C 2011 Mesoporous Silicon Anodes Prepared by Magnesiothermic Reduction for Lithium Ion Batteries *Journal of the Electrochemical Society* **158** A1055-A9

[74] Li C, Fang G, Sheng S, Chen Z, Wang J, Ma S and Zhao X 2005 Raman spectroscopy and field electron emission properties of aligned silicon nanowire arrays *Physica E: Low-dimensional Systems and Nanostructures* **30** 169-73
[75] Lim J, Hippalgaonkar K, Andrews S C, Majumdar A and Yang P 2012 Quantifying surface roughness effects on phonon transport in silicon nanowires *Nano letters* **12** 2475-82
[76] Piscanec S, Cantoro M, Ferrari A, Zapien J, Lifshitz Y, Lee S, Hofmann S and Robertson J 2003 Raman spectroscopy of silicon nanowires *PHYSICAL REVIEW-SERIES B-* **68** 241312 (R)- (R)
[77] Glynn C, Lotty O, McSweeney W, Holmes J D and O'Dwyer C 2011 Raman Scattering Spectroscopy of Metal-Assisted Chemically Etched Rough Si Nanowires *ECS Transactions* **35** 73-86